

Reflection Nebula Visualization

Marcus A. Magnor*
MPI Informatik

Kristian Hildebrand
MPI Informatik

Andrei Lintu
MPI Informatik

Andrew J. Hanson†
Indiana University

ABSTRACT

Stars form in dense clouds of interstellar gas and dust. The residual dust surrounding a young star scatters and diffuses its light, making the star’s “cocoon” of dust observable from Earth. The resulting structures, called *reflection nebulae*, are commonly very colorful in appearance due to wavelength-dependent effects in the scattering and extinction of light. The intricate interplay of scattering and extinction cause the color hues, brightness distributions, and the apparent shapes of such nebulae to vary greatly with viewpoint. We describe here an interactive visualization tool for realistically rendering the appearance of arbitrary 3D dust distributions surrounding one or more illuminating stars. Our rendering algorithm is based on the physical models used in astrophysics research. The tool can be used to create virtual fly-throughs of reflection nebulae for interactive desktop visualizations, or to produce scientifically accurate animations for educational purposes, e.g., in planetarium shows. The algorithm is also applicable to investigate on-the-fly the visual effects of physical parameter variations, exploiting visualization technology to help gain a deeper and more intuitive understanding of the complex interaction of light and dust in real astrophysical settings.

CR Categories: I.3.3 [Computer Graphics]: Picture/Image Generation—Viewing algorithms; I.3.7 [Computer Graphics]: Three-Dimensional Graphics and Realism—Color, shading, shadowing, and texture; J.2 [Computer Applications]: Physical Sciences and Engineering—Astronomy

Keywords: volume rendering, global illumination, dust, nebula, astronomy

1 INTRODUCTION

Reflection nebulae are among the most colorful objects in the night sky, Fig. 1, which is why science fiction movies and popular science journals frequently feature pictures of these captivating interstellar entities. Besides their aesthetic appeal, reflection nebulae also have considerable scientific relevance. They are the birth places of new stars, and their astrophysical study reveals new insights into star formation and stellar composition. Interesting physics is also responsible for the colorful visual appearance of reflection nebulae. The intricate interplay of wavelength-dependent light scattering and extinction gives rise to large variations in color hue and brightness. Depending on the viewpoint, reflection nebulae exhibit wide variations in appearance; unfortunately, we cannot witness these variations directly for any single nebula because, since our observational vantage point is fixed on or near the Earth, we cannot appreciably change our viewing angle. This makes virtual tours of reflection nebulae a popular target of virtual astronomy animations. 3D tours of astronomical nebulae in current planetarium shows typically begin from real observational data, and include varying de-

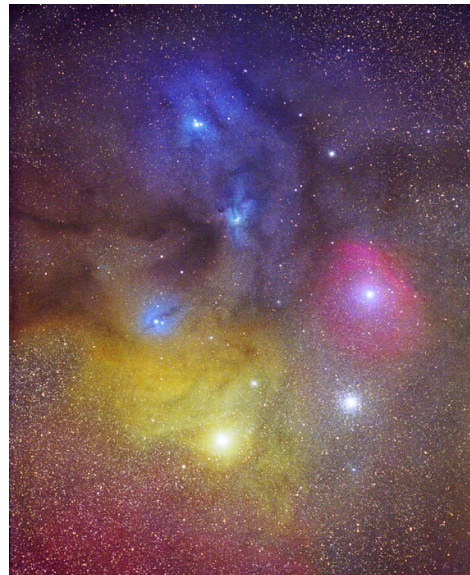


Figure 1: Reflection nebulae: Recently formed, hot stars illuminate the surrounding interstellar dust that scatters and absorbs the star light to give rise to a large range of color hues and brightness variations. (*Rho Ophiuchi region*, from [28], © T. and D. Hallas)

grees of artistic work to generate the views from non-Earth viewpoints [20, 6, 5, 19, 8]. To authentically reproduce the dependence of a nebula’s appearance on viewpoint and dust distribution, however, substantial scientific modeling work must be done to faithfully represent the physical environment. Accurate, physics-based 3D visualizations of reflection nebulae are also needed for educational purposes if the goal is to gain a deeper understanding of the complex interactions of light and dust in interstellar space.

Here we propose a significant extension to the current approach to 3D modeling and visualization of reflection nebulae. Based on the same physical models that are used in astrophysics research, we present an interactive visualization tool for arbitrary three-dimensional dust distributions surrounding one or more illuminating stars. Anisotropic scattering characteristics, wavelength dependence, multiple scattering, and trajectory-dependent extinction are taken into account. Besides supplying faithful renderings, our system also supports exploring the visual effects of changing a nebula’s physical parameters, an essential visualization function for astrophysical hypothesis checking. The visualization tool can be used in conjunction with synthetic 3D nebula models as well as dust distributions derived from real nebulae, allowing for artistic freedom and scientific rigor at the same time.

In the following Section, we review related previous work. After an introductory overview of the fundamental physics of reflection nebulae in Section 3, we describe our visualization model in Section 4. Section 5 highlights the interactive rendering algorithm and its implementation in graphics hardware. We present visualization results and discuss our approach in Section 6, before we conclude with an outlook on future extensions in Section 7.

*e-mail: magnor@mpi-sb.mpg.de

†e-mail: hanson@cs.indiana.edu

2 RELATED WORK

While tools for visualizing astrophysical simulation results are in common use, only a few publications address visually realistic, physics-based rendering techniques of actual astronomical objects. Nadeau et al. at the San Diego Supercomputer Center (SDSC) created a fly-through animation of the Orion Nebula for the Hayden Planetarium in New York [20, 19, 8]. The nebula model was based on astrophysical analysis of decades of observational data [32]. Rendering the final, 150-second animation at high resolution took 12 hours on SDSC’s IBM RS/6000 SP supercomputer using 952 processors [20]. More recently, Magnor et al. reconstructed and rendered 3D models of planetary nebulae [17]. This work applied emissive volume rendering to interactively visualize the ionized gas on conventional PC graphics hardware. In contrast to planetary nebulae consisting of glowing gas, however, the reflection nebulae considered here do not directly emit visible light. Instead, light from one or more nearby stars is scattered and absorbed by interstellar dust in the stellar neighborhood. While the appearance of a planetary nebula varies with changing viewpoint only in shape and brightness distribution, reflection nebulae additionally change in color due to wavelength-dependent scattering and extinction. This physically different, and considerably more complex, illumination mechanism requires a rendering algorithm for reflection nebulae that accurately takes wavelength-dependent scattering and extinction properties of interstellar dust into account.

In 1938, Henyey and Greenstein derived analytical expressions for the color and brightness distributions of reflection nebulae for idealized geometrical configurations [11]. Their optical model of reflection nebulae is generally accepted in astrophysics [31, 30, 26, 2, 9, 10] and forms the basis of our rendering algorithm.

In volume rendering terms, a reflection nebula constitutes a participating medium. Volume rendering techniques have been proposed that take into account volumetric absorption and anisotropic scattering characteristics [18] as well as the effects of multiple scattering [24, 14, 27]. More recently, advanced algorithms have been presented to better approximate global illumination effects, either for general visualization purposes [15], or to obtain more realistic rendering results of natural phenomena exhibiting volumetric scattering characteristics [13, 22, 23]. Similar to Riley et al. [23], our visualization approach is based on pre-computing multiple-scattering phase functions and tabulating angle-dependent scattering probabilities. Our method can be employed in conjunction with any arbitrary, even experimentally measured, single-particle phase function because we rely on full Monte-Carlo simulations to derive multi-scattering probability density distributions prior to rendering. To be able to pre-compute local illumination per volume element, star illumination geometry and dust distribution are kept fixed. During rendering, viewpoint and viewing direction are freely and interactively navigatable all around as well as through the nebula volume. Our interactive visualization algorithm builds on recent work in ray-based direct volume rendering exploiting modern PC graphics hardware [16, 25], to which we additionally introduce a hierarchical multi-resolution approach to reproduce large-scale global illumination effects.

3 REFLECTION NEBULAE

Reflection nebulae are clouds of gas and dust that lie in the vicinity of one or more stars, Fig. 1. By scattering the star’s light in all directions, the dust becomes visible to us. Besides scattering, interstellar dust also absorbs an appreciable amount of the incident light. In regions of high dust density, most light from beyond the dust cloud is absorbed, forming a so-called *dark nebula*, Fig. 2.

Reflection nebulae are often associated with very hot stars of spectral class O or B [1]. Because such hot stars have only a short

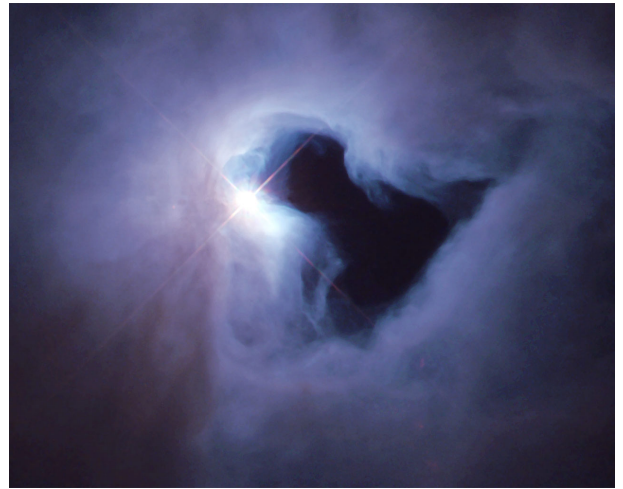


Figure 2: NGC 1999: A recently formed hot star illuminates the surrounding interstellar dust that scatters and absorbs the star light to create a colorful reflection nebula. (from [7] © NASA/STScI)

life span (on the order of 10^6 years in comparison to 10^{10} years for our Sun), they must have formed only recently, leading to the conclusion that a reflection nebula represents the remains of the star’s protostellar cloud.

3.1 Interstellar Dust

The space between stars is not entirely empty, but is filled with very low density, yet rather filthy, smoke-like gas. If interstellar material were compressed to the density of air, objects would disappear in the haze at a distance of less than one meter [1]. This interstellar dust stems predominantly from so-called asymptotic giant branch (AGB) stars, evolved and comparatively cool stars whose stellar wind carries with it large amounts of carbon and silicates from the stars’ surface. This stellar “soot” is a mixture of a variety of chemical compounds and represents an ensemble of various different dust particles whose individual dust grain size varies roughly between 100nm and $1\mu\text{m}$.

The scattering properties of a single particle are accurately described by Mie scattering theory [29]. To describe the net optical effect of the very large number of different dust grains illuminated by polychromatic, unpolarized light, astrophysicists frequently resort to only two (weakly wavelength-dependent) scalar parameters: the ensemble values for the *albedo* and for the *single-particle scattering anisotropy* of the dust [3, 31, 10]. It turns out that these two parameters suffice to correctly characterize the optical properties of interstellar dust to within today’s observational accuracy.

The albedo $a = [0, 1]$ is the ratio of radiosity to irradiance, i.e., the average percentage of radiation incident on a dust particle that is being scattered. If the dust is completely black and all incident light is absorbed, its albedo is zero. In the other extreme, all incident radiation is scattered and the albedo value is one. From the average absorption coefficient σ_{abs} and scattering coefficient σ_{sct} , dust albedo is defined as

$$a = \frac{\sigma_{\text{sct}}}{\sigma_{\text{abs}} + \sigma_{\text{sct}}} = \frac{\sigma_{\text{sct}}}{\sigma_{\text{ext}}}.$$

Absorption and scattering together give rise to light extinction in turbid media, so the sum of both yields the extinction coefficient $\sigma_{\text{ext}} = \sigma_{\text{abs}} + \sigma_{\text{sct}}$.

The size of interstellar dust grains is roughly on the order of the wavelength of visible light. This leads to anisotropic scattering,

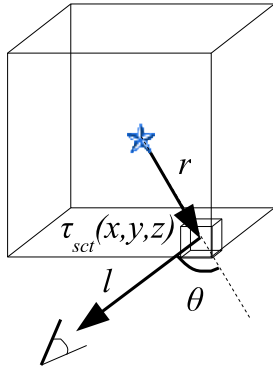


Figure 3: Nebula model: The nebula volume is discretized into voxels. Each voxel receives direct light from the star, attenuated along the distance r . Part of the illuminating light is scattered towards the observer, depending on the scattering depth τ_{sct} at the voxel (x, y, z) as well as the angle θ between view direction and radial illumination vector. As it traverses the path l from the voxel to the observer, the scattered light undergoes further extinction.

i.e., the scattering probability is direction-dependent. For spherical particles and unpolarized light, scattering is symmetric around the incident radiation direction, so scattering probability varies only with deflection angle θ , Fig. 3. In astrophysics research, the phase function of interstellar dust is frequently modeled using an analytic expression proposed by Henyey and Greenstein [12]:

$$p(\theta) = \frac{1 - g^2}{2(1 + g^2 - 2g \cos \theta)^{3/2}}. \quad (1)$$

The Henyey-Greenstein phase function has only one free parameter g . This *anisotropy factor* g denotes the cosine of the mean scattering angle. For a given value of $g \in [-1, 1]$, (1) yields the probability distribution p as a function of scattering angle θ .

Observations have shown that, within measurement error margins, the optical properties of interstellar dust are the same throughout the galaxy [10]. At visible wavelengths, the albedo is $a \approx 0.6$, and the scattering anisotropy factor is $g \approx 0.6$ [31, 10]. While albedo and scattering anisotropy are more or less constant at visible wavelengths, the scattering coefficient σ_{sct} varies appreciably with wavelength. While blue light is scattered almost twice as often as red light, the exact ratio of scattering probability at red and blue wavelengths varies somewhat for different regions in the Galaxy [1].

3.2 Color

In astrophysical settings, object color is commonly referred to in terms of band-filtered observations. The Johnson color system features three bands in the visible range of the spectrum that approximately correspond to the RGB colors in computer graphics. The peak filter wavelengths and half-maximum pass bandwidths are $445 \pm 47\text{nm}$ for the blue (*B* band), $551 \pm 44\text{nm}$ for the green (visible, *V* band), and $658 \pm 69\text{nm}$ for the red (*R* band) spectral region [1].

Because the scattering coefficient σ_{sct} varies with wavelength, extinction is also wavelength-dependent. The *extinction* A , *extinction depth*, or *optical depth* $\tau_{\text{opt}} = A = \sigma_{\text{ext}} \cdot l$ is the product of total path length l and the average extinction coefficient σ_{ext} along the way, Fig. 3. To express the relative amount of extinction A at different wavelengths λ , the *ratio of total to selective visual extinction* R_V is frequently used in astrophysics. It is related to the slope of the extinction curve $A(\lambda)$ near the *V* band (green).

Cardelli et al. [3] give an empirical formula to find the extinction A for the *U* and *R* band relative to the *V* band for arbitrary R_V values. For the standard value $R_V = 3.1$, relative extinction factors are $A_B/A_V = 1.324$ and $A_R/A_V = 0.748$ [1]. In dense clouds, however, $R_V \approx 5$ which yields $A_R/A_V = 0.8$ and $A_B/A_V = 1.2$, i.e. scattering increases more slowly with decreasing wavelength, hinting at a slightly larger average particle size. In summary, an individual, average interstellar dust grain scatters light predominantly in the forward direction ($g > 0$) and is made up of grayish material ($a < 1$, $\sigma_{\text{abs}}(\lambda) \approx \text{const}$). Because scattering probability increases with decreasing wavelength, scattered light is bluer than the incident light, while transmitted, unscattered light becomes redder.

Because dust concentrations in reflection nebulae can reach high densities, the illuminating star light may be scattered not only once, but multiple times. The *scattering depth* $\tau_{\text{sct}} = \sigma_{\text{sct}} l$ denotes the average number of scattering events that a photon undergoes along a travel path length l . It is directly proportional to dust particle density. For albedo values $a < 1$, multiple scattering causes the scattered light to diminish because at each scattering event, a fraction $(1 - a)$ of the incident light is absorbed. After n scattering events, only a^n of the initial illuminating radiance is still present. Overall scattering anisotropy also decreases with g^n , so that after several scattering events, the scattered light is in essence distributed isotropically over all directions.

To account for multiple scattering exactly, full-fledged, computationally very expensive radiative transfer simulations are required. Alternatively, we propose a hierarchical multi-resolution strategy to take multiple scattering into account, Section 4.2. This enables us to faithfully render nebulae at interactive frame rates without serious impact on the overall accuracy of the appearance for most situations.

4 VISUALIZATION MODEL

We discretize the volume of the reflection nebula into volume elements (voxels). Each voxel is assigned its individual scattering depth $\tau_{\text{sct}} = \sigma_{\text{sct}} l$, where l is the linear size of the voxel, and the scattering coefficient σ_{sct} is directly proportional to local dust density. Let us assume that one illuminating star is located at the center of the volume, as shown in Fig. 3. The radiance received by a voxel located at a point (x, y, z) a distance r from the star depends on the star's radiant power Φ_{star} and the optical depth $\tau_{\text{opt}} = \tau_{\text{sct}}/a$ accumulated along the way:

$$L_{\text{ill}} = \frac{\Phi_{\text{star}}}{4\pi r^2} e^{-\int_0^r \tau_{\text{opt}}(r')/r dr'}. \quad (2)$$

Voxel illumination L_{ill} does not change with viewpoint, so it can be pre-computed for each voxel, subject to the constraint that dust distribution and illumination geometry stay fixed. Of the illuminating radiance reaching a voxel, a fraction $P(\tau_{\text{sct}}, \theta)$ is scattered in the observer's direction,

$$L_{\text{sct}} = L_{\text{ill}} \cdot P(\tau_{\text{sct}}, \theta). \quad (3)$$

The scattered light L_{sct} must then still travel the path l from the voxel to the observer, along which the light is again attenuated:

$$L_{\text{obs}} = L_{\text{sct}} e^{-\int_0^l \tau_{\text{opt}}(l')/l dl'}. \quad (4)$$

Total observed radiance is derived by summing up L_{obs} from all voxels along each line of sight. The scattering and extinction calculations must be performed for the red, green, and blue channel separately because σ_{ext} and τ_{sct} vary with wavelength, Section 3.2.

To render a reflection nebula that is lit by more than one star, per-voxel illumination (2) is pre-computed for each illuminating star

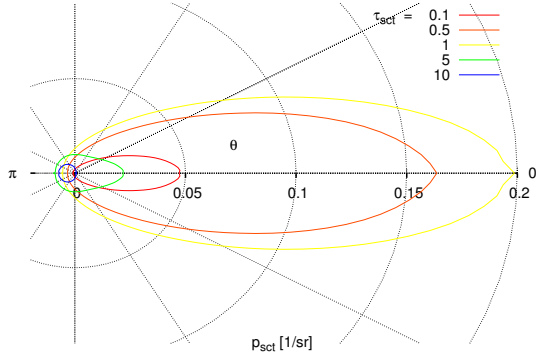


Figure 4: Directional scattering probability of a voxel $P(\tau_{\text{sct}}, \theta)$ with albedo $a = 0.6$ and anisotropy factor $g = 0.6$ employing the Henyey-Greenstein phase function [12]. The forward scattering direction is to the right ($\theta = 0$). With increasing scattering depth τ_{sct} , overall scattering first increases, then decreases again. Relative forward scattering also decreases until for the highest scattering depth $\tau_{\text{sct}} = 10$, more light is actually being scattered backward than forward due to extinction within the voxel volume.

separately. During rendering, the scattered radiance per voxel (3) is evaluated for all stars. Thanks to the superposition principle, the contributions from all stars to the per-voxel scattered radiance can be simply summed before computing the observed radiance (4).

4.1 Voxel Scattering Characteristics

The fraction $P(\tau_{\text{sct}}, \theta)$ of illumination radiance that is scattered from the voxel into the viewing direction depends on the scattering depth τ_{sct} (i.e., dust density) of the voxel as well as on the deflection angle θ between the incident ray from the star and the viewing direction, Fig. 3. Because dust density can be so high that an illuminating photon is likely to be scattered several times within the voxel before exiting, multiple scattering must be taken into account when deriving $P(\tau_{\text{sct}}, \theta)$. We use Monte-Carlo simulation to pre-compute and tabulate scattering probabilities $P(\tau_{\text{sct}}, \theta)$ for 1000 scattering depth values between $\tau_{\text{sct}} = 0$ and 10, each for 72 directions between $\cos \theta = -1$ and $+1$. The Appendix gives details of the Monte-Carlo simulation. The table is run for the albedo and anisotropy values $a = 0.6$, $g = 0.6$ of interstellar dust, as suggested by the astrophysics literature [10]. To explore the effects of albedo and anisotropy variations on reflection nebula appearance, we also compute tables for different albedo and anisotropy values. While we employ here the Henyey-Greenstein phase function (1), note that our approach can be used in conjunction with any arbitrary single-particle phase function.

Fig. 4 depicts the direction-dependent scattering probability distribution of a voxel for different scattering depths τ_{sct} . Due to multiple scattering, directional dependence changes drastically with voxel scattering depth. With increasing dust concentration, the total amount of scattered light first increases, then starts to decrease for very dense dust. Regions of thin to moderate dust are dominated by forward scattering, while very dense dust regions exhibit mostly backward scattering.

The combined effects of anisotropy, multiple scattering, absorption, wavelength dependence, and geometric configuration on reflection nebula appearance is illustrated in Fig. 5. The otherwise empty nebula volume is initialized by setting the voxels in the front-most layer, as seen from the observer, and the layer on the far side of the illuminating star to non-zero scattering depth values. Scattering depth increases with angle. A thin veil of dust appears bluer than the illuminating star, whether the dust is in front of or behind the

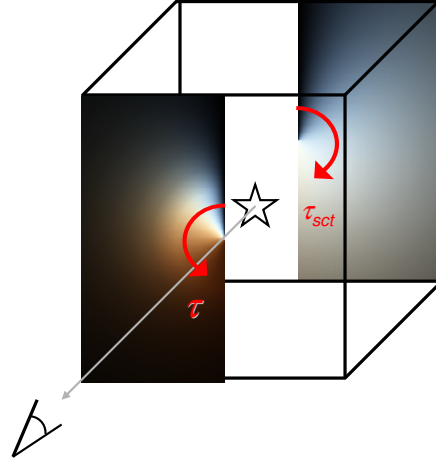


Figure 5: Color variations in reflection nebulae as a function of geometric configuration and scattering depth τ_{sct} . The scattering depth is constant in the radial direction and increases with angle from the top ($\tau_{\text{sct}} = 0$) to the bottom ($\tau_{\text{sct}} = 10$). The illuminating star light is white.

star. With increasing scattering depth, however, extinction affects blue light more strongly than red light, and the light passing through the dust from the star to the viewer becomes redder and dimmer. In contrast, the light reflected back from the dust behind the star takes on the color of the illuminating star while its brightness asymptotically reaches a fixed level. These findings are in accordance with analytical considerations [11]. The contrast in Fig. 5 has been optimized to bring out the color changes. In reality, thin dust in front of the star appears much brighter than dust behind it due to forward scattering, as is obvious from Fig. 4.

4.2 Multiple Scattering

Using Monte-Carlo simulation to determine the scattering probability distribution $P(\tau_{\text{sct}}, \theta)$, we can correctly account for multiple scattering on a local, per-voxel level. Photons that leave a voxel but are scattered back into it from neighboring regions, however, are not taken into account this way. Note that these neglected multiply-scattered photons can only increase overall observed radiance L_{obs} .

To faithfully reproduce the wide-range effect of multiple scattering, we pursue a hierarchical approach, Fig. 6. During pre-computation, the full-resolution voxel model V_0 is down-sampled n times along all three dimensions. For each downsampling step, the scattering depths τ_{sct} from eight neighboring voxels are averaged, and twice this average value is assigned to the corresponding lower-resolution voxel. The factor of two comes from the doubled linear size of the lower-resolution voxel. For each volume resolution V_i , we also pre-compute voxel illumination, (2).

During visualization, we render a resolution pyramid of images I_i , $i = 0, \dots, n$, each obtained from the corresponding volume representation V_i , Fig. 6. We then down-sample the rendered images I_i to obtain \bar{I}_{i+1} . Note that the images I_j and \bar{I}_j have the same resolution but are generated from different-resolution volumes V_j and V_{j-1} , respectively. I_j includes the effect of photons that at resolution level V_{j-1} exit a voxel but are scattered back into it from one of the adjacent voxels. I_j is therefore a little brighter than \bar{I}_j . Because multiple scattering can only add to observed radiance, the difference image

$$\Delta I_j = I_j - \bar{I}_j$$

is clipped to non-negative values and up-sampled to obtain $\Delta \hat{I}_{j-1}$.

Starting from the second-lowest resolution level considered, the up-sampled difference image $\Delta\hat{I}_i$ is added to the difference image of the corresponding resolution level ΔI_i to obtain

$$\Delta I_i^* = \Delta\hat{I}_i + \Delta I_i .$$

The difference image ΔI_i^* is repeatedly up-sampled and combined with ΔI_i for all resolution levels $i > 0$ until the full-resolution level $i = 0$ is reached. The final image I is obtained by adding the accumulated difference image to the image rendered from the full-resolution volume: $I = I_0 + I_0^*$. This final image includes the effect of multiple scattering up to the scale length of the lowest resolution level taken into account.

Fig. 7 depicts the effect of wide-range multiple scattering at different scale lengths in forward and backward scattering direction. For a homogeneous, planar layer of dust in front of the illuminating star, global multiple scattering noticeably increases nebula surface brightness. Also, nebula color becomes more bluish because of the monotonically increasing scattering probability with shorter wavelength. For dust on the star’s far side, on the other hand, wide-range multiple scattering has only little effect.

We remark that the described approach assumes that a homogeneous and a non-homogeneous dust distribution of the same average density both yield the same average scattered radiance. Strictly speaking, this assumption is valid only for smoothly varying dust concentrations. In regions dominated by strong density gradients the approach still yields qualitatively plausible results, but, of course, our method cannot substitute for full radiative transfer simulations in the general case.

4.3 Nebula Generation

Our visualization tool can render realistic views of any given 3D dust distribution. For planetarium shows, the generation of a specific reflection nebula may be driven by artistic and esthetic design criteria, while in an astrophysical setting, the dust distribution may be intended to reproduce the measured experimental brightness distribution of some real nebula.

For the former case, we found that the following recipe generates natural-appearing synthetic reflection nebulae. In accordance

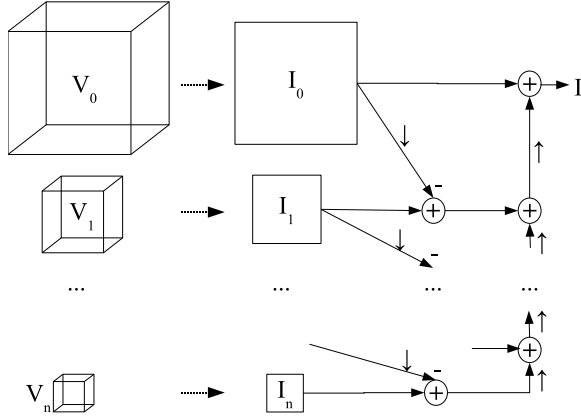


Figure 6: Multi-resolution rendering to incorporate the global effect of multiple scattering on nebula appearance: A resolution pyramid of images I_i is rendered from the mipmap representation V_i of the nebula volume. Images from one resolution level are down-sampled (\downarrow) and subtracted from the images rendered at the next-lower resolution. From the lowest-resolution level upwards, the difference images are subsequently up-sampled (\uparrow) and summed. The accumulated difference image is added to the full-resolution image I_0 to yield the resulting image I .



Figure 7: Effect of wide-range multiple scattering: a homogeneous layer of dust in front of (upper row) and behind an illuminating central star (lower row) is rendered, taking into account $n = 0, 1, 2$ resolution levels (left to right).

with the physical processes accompanying star formation, we assume that stellar winds from the illuminating star have swept clean the immediate surroundings, so that the star is situated within a bubble of relatively low dust concentration. The swept-up dust accumulates along the edge of the bubble where, accordingly, dust density increases sharply. Beyond the bubble, dust concentration falls off exponentially with increasing radial distance. Since stars typically form in very large interstellar clouds, and because reflection nebulae are visible only around stars that form near the edge of such a cloud, the far side of the nebula volume is filled with high-density, optically dense interstellar dust. Because the dust along the edge of the bubble has been swept up by hydrodynamic stellar wind processes, dust concentration is not homogeneous. To mimic corresponding variations in local dust density, we use 3D Perlin noise [21] to modulate voxel scattering depth $\tau_{\text{sct}}(x, y, z)$. A wide variety of different-looking, yet realistically appearing nebulae can be created by varying Perlin noise amplitude and frequency, Fig. 11.

5 INTERACTIVE RENDERING

Prior to visualization, the pre-computed scattering table is uploaded as a 2D floating-point texture to graphics memory. A floating-point 3D texture stores the scattering depth τ_{sct} for each voxel. Depending on the number of illuminating stars, one or more 3D arrays store the pre-computed illumination L_{ill} for each voxel. Additionally, emissive radiance L_{em} is stored per voxel. The 3D emission texture allows us to simulate ionized, glowing gas clouds that may be intermixed with the interstellar dust, as well as to visualize the illuminating star. Ionized gas radiates isotropically in all directions, so L_{em} can be added directly to the scattered radiance L_{sct} in (3). Both contributions undergo the same extinction on the way from the voxel to the observer L_{obs} , (4).

Our reflection nebula visualization algorithm is based on GPU-based ray-casting. After determining viewing ray parameters as described in [16], we use a fragment program to step along each viewing vector from front to back in voxel-length intervals. At each step, we look up local scattering depth τ_{sct} , voxel illumination L_{ill} , and emissive RGB radiance values L_{em} from the 3D volume textures, taking advantage of hardware-accelerated trilinear interpolation. The fragment program computes the angle between viewing ray direction and the incident star-light direction θ , and queries the scattering probability table to determine $P(\tau_{\text{sct}}, \theta)$. Equation (3) is evaluated, and the emissive radiance L_{em} is added. If more than one star illuminates the dust cloud, scattered radiance is evaluated for each star and summed up per voxel. Rendering times and memory requirements increase linearly with the number of stars.

To quickly compute (4), we accumulate extinction depth τ_{opt}



Figure 8: Left: Photo (color composite) of the “Cocoon” reflection nebula IC 5146 (from [4], © Greg Crinklaw); right: rendering result for a simulated dust distribution with 4 illuminating stars, composited into a star field photo for enhanced visual realism.

while stepping along the ray. For each ray, extinction depth τ_{sct} is initialized either to zero or to a fixed offset in case we wish to include interstellar extinction outside the nebula. At each step i along the viewing ray, local extinction is added up, $\tau_{\text{opt}}^{i+1} = \tau_{\text{opt}}^i + \tau_{\text{sct}}^{i+1}/a$. Equation (4) can then be quickly evaluated. Note that (3) and (4) are actually computed for the red, green, and blue channel separately by weighting τ_{sct} according to Section 3.2. To take large-scale global illumination effects into account, the hierarchical multi-resolution algorithm described in Section 4.2 is implemented to run entirely on the GPU. For display, the rendered image is optionally normalized and gamma-corrected.

To interactively explore the effects of different physical parameters on nebula appearance, fragment shader constants like star color, ratio of total-to-selective visual extinction R_V , and albedo can be changed on the fly. We can upload scattering tables computed for different albedo and anisotropy values as well as for arbitrary phase functions. The result is an artificial but physically plausible rendition of the reflection nebula.

The change in appearance due to different viewing directions can be evaluated by simply rotating the nebula. However, to appreciate the full range of color variations, e.g., for planetarium shows, we want to be able to move the viewpoint inside the nebula. By moving the viewpoint through the dust towards the star, previously dark clouds become transparent and overall reddening decreases until the bluish tint of backscattered starlight dominates. We appropriately modify the original GPU-based ray-casting algorithm [16, 25] to solve the problem that arises when the near clipping planes fall within the volume.

6 RESULTS

Our visualization tool is designed to render realistic images of reflection nebulae. A side-by-side comparison of a photo composite of an actual nebula (IC 5146) and the visualization of a simulated dust distribution is shown in Fig. 8. Note how our rendering algorithm produces color hues very similar to reality, and how our synthetically generated dust distribution convincingly mimics overall appearance of the real nebula. The importance of multiple scattering on large scales can be seen in Fig. 9. The increase in nebula surface brightness with hierarchy levels included suggests that we are looking at rather thin dust that is situated in front of the illuminating star. Fig. 10 presents screenshots from a fly-around and a fly-through sequence for two synthetic nebulae to illustrate the change in shape and color with viewpoint. From the outside, the nebula appears reddish with dark regions of dense dust. Once inside the nebula, backscattered light is responsible for the blue-enhanced appearance. The wide variety in shape and color of re-

flexion nebulae following from dust density distribution is illustrated in Fig. 11. Depending on dust concentration and geometric dust configuration, the scattered star light reaches the viewpoint almost unhindered (bluish appearance), attenuated to varying degrees (reddish appearance), or not at all (dark regions).

In addition to physical visualizations, we can also explore the influence of varying different physical parameters on nebula appearance. The images in Fig. 12 show the same nebula from the same viewpoint, but for different parameter settings. The astrophysically correct reference image is depicted in Fig. 12(a). Fig. 12(b) illustrates nebula appearance if the dust in the nebula behaves more like galactic dust, i.e., $R_V = 3.1$. Because for $R_V = 3.1$, relative extinction rises more steeply with decreasing wavelength than for $R_V = 5$, nebula colors are somewhat more vivid. In reality, reflection nebulae are associated with hot O or B stars. In our visualization tool, however, we can exchange the illuminating star, e.g., for our own Sun, Fig. 12(c). The cooler star temperature causes the entire nebula to appear redder. Finally, we can vary the scattering and absorption properties of the interstellar dust grains. For an increased albedo value, the entire nebula becomes brighter, Fig. 12(d). By enhancing forward scattering characteristics, Fig. 12(e), already bright regions become brighter, while overall contrast increases. In conjunction with known dust configurations of actual nebulae, studying the effects of dust albedo and scattering anisotropy on nebula appearance with our visualization tool helps to understand the optical properties of interstellar dust [10].

In the presence of one illuminating star and with multi-resolution rendering turned off, our rendering algorithm performs at 7.5 frames per second on an nVidia GeForce 6800 Ultra graphics board, rendering at 512×512 -pixel resolution from a 128^3 -voxel model. With multi-resolution rendering turned on, rendering frame rate drops to 6.1 frames per second, taking 3 resolution levels into account. Alternatively, for 2,3,4 or 5 illuminating stars, rendering frame rates are 4.7, 3.6, 2.5, and 1.9 Hz, respectively.

7 CONCLUSIONS

We have presented an interactive visualization tool to realistically render reflection nebula appearance from physical principles. The algorithm runs on conventional hardware and allows the user to interactively vary viewing position and direction as well as to change physical parameters of the nebula. Multiple scattering is taken into account locally as well as on large scales. Our visualization tool can be used to create virtual fly-throughs of reflection nebulae for interactive desktop visualizations, or to produce scientifically accurate animations for educational purposes. By varying physical parameter values, the algorithm can be used to visualize and validate hypothetical models for observed data.

Next, we want to use our algorithm to recover the 3D shape of actual nebulae. We intend to make use of additional observations in the infrared [3] to be able to better constrain the reconstruction problem. To recover both the gas and the dust component of gaseous nebulae, we will include emission-line images in addition to color-bandpass images. By concentrating first on planetary nebulae, additional geometric constraints can be exploited [17].

APPENDIX: MONTE-CARLO SIMULATION OF ANISOTROPIC PHOTON SCATTERING

Let the simulation consider N photons. Each photon is initialized with a weight $w_0 = 1/N$. Instead of a cube of edge length l , a voxel is modeled as a sphere of the same volume. The scattering coefficient is $\sigma_{\text{sct}} = \tau_{\text{sct}}/l$. The photon is placed on the sphere at \mathbf{x}_0 with its travel direction \mathbf{d}_0 pointing towards the sphere’s center. In the following, the photon is traced through the volume until it either emerges from the sphere, in which case its remaining weight w_i is

added to the appropriate direction bin $B[\cos \theta]$ of its emergence angle $\cos \theta = \mathbf{d}_i \cdot \mathbf{d}_0$, or its weight w_i falls below a minimum threshold and the photon is discarded. Given a uniformly distributed (pseudo-) random variable $u = [0, 1]$, the next scattering event of the photon takes place after it has travelled a length

$$r = -\ln(1 - u) / \sigma_{\text{sct}},$$

where $\sigma_{\text{sct}} = 1/\bar{r}$ is the scattering coefficient. From the previous position \mathbf{x}_i and direction \mathbf{d}_i , the new scattering site's 3D coordinates are

$$\mathbf{x}_{i+1} = \mathbf{x}_i + r \cdot \mathbf{d}_i.$$

To determine the new scattering direction \mathbf{d}_{i+1} , scattering anisotropy must be taken into account. We are free to use any analytic or measured single-particle phase function. Here, we rely on the Henyey-Greenstein phase function (1), adopted from astrophysics research. For (1), the cumulative distribution function can be inverted analytically to yield

$$\cos \theta = \frac{1}{2g} \cdot \left(1 + g^2 - \left(\frac{1 - g^2}{1 - g + 2gv} \right)^2 \right)$$

if $g \neq 0$, i.e., for non-isotropic scattering. In azimuthal angle ϕ , scattering probability is constant,

$$\phi = 2\pi \cdot w.$$

Both random variables $v, w = [0, 1]$ are uniformly distributed.

To compute the new scattering direction $\mathbf{d}_{i+1} = (d'_x, d'_y, d'_z)$ in Cartesian coordinates, two cases must be distinguished. If the previous photon direction $\mathbf{d}_i = (d_x, d_y, d_z)$ was almost parallel to the z -axis, e.g., $\|d_z\| > 0.9999$, then

$$\begin{aligned} d'_x &= \sin \theta \cos \phi \\ d'_y &= \sin \theta \sin \phi \\ d'_z &= \frac{d_z}{\|d_z\|} \cdot \cos \theta, \end{aligned}$$

otherwise

$$\begin{aligned} d'_x &= \frac{\sin \theta}{\zeta} \cdot (d_x d_z \cos \phi - d_y \sin \phi) + d_x \cos \theta \\ d'_y &= \frac{\sin \theta}{\zeta} \cdot (d_y d_z \cos \phi + d_x \sin \phi) + d_y \cos \theta \\ d'_z &= -\zeta \sin \theta \cos \phi + d_z \cos \theta \end{aligned}$$

with $\zeta = \sqrt{1 - d_z^2}$. The photon weight is multiplied by the albedo, $w_{i+1} = w_i \cdot a$. The photon is traced until it either leaves the sphere, or until its weight w_i falls below a preset threshold. The simulation ends after simulating all N photons. The accumulated values in the bins, $B[\cos \theta]$, represent the row of entries for τ_{sct} in the scattering probability table $P(\tau_{\text{sct}}, \theta)$.

REFERENCES

[1] J. Binney and M. Merrifield. *Galactic Astronomy*. Princeton University Press, 1998.

[2] D. Calzetti, R. Bohlin, K. Gordon, A. Witt, and L. Bianchi. Scattering properties of the dust in the reflection nebula IC 435. *Astrophysical Journal*, 446:L97–L100, June 1995.

[3] J. Cardelli, G. Clayton, and J. Mathis. The relationship between infrared, optical, and ultraviolet extinction. *Astrophysical Journal*, 345:245–256, 1989.

[4] G. Crinklaw. Cocoon nebula (IC 5146, OCL 213). <http://www.skyhound.com/sh/archive/sep/Cocoon.html>, 2005.

[5] Donald Davis. Space artist and planetarium animation specialist. <http://www.donaldedavis.com/>. private e-mail conversation.

[6] Evans and Sutherland. Wonders of the universe – planetarium show, 2000. http://www.es.com/products/digital_theater/wonders_2.jpg.

[7] NASA/ESA Hubble Heritage Image Gallery. NGC 1999. <http://heritage.stsci.edu/gallery/wallpaper/2000-10/>, 2005.

[8] J. Genetti. Volume-rendered galactic animations. *Communications of the ACM*, 45(11):62–66, November 2002.

[9] S. Gibson and K. Nordsieck. The Pleiades reflection nebula. II. simple model constraints on dust properties and scattering geometry. *Astrophysical Journal*, 589:362–377, May 2003.

[10] K. Gordon. Interstellar dust scattering properties. In A. Witt, G. Clayton, and B. Draine, editors, *Astrophysics of dust*, ASP conference series, 2004.

[11] L. Henyey and J. Greenstein. The theory of the colors of reflection nebulae. *Astrophysical Journal*, 88:580–604, 1938.

[12] L. Henyey and J. Greenstein. Diffuse radiation in the galaxy. *Astrophysical Journal*, 93:70–83, 1941.

[13] H. W. Jensen, S. Marschner, M. Levoy, and P. Hanrahan. A practical model for subsurface light transport. In *Proc. ACM Conference on Computer Graphics (SIGGRAPH '01)*, pages 511–518, 2001.

[14] J. Kajiya and B. von Herzen. Ray tracing volume densities. *Proc. ACM Conference on Computer Graphics (SIGGRAPH'84)*, pages 165–174, July 1984.

[15] J. Kniss, S. Premoze, C. Hansen, P. Shirley, and A. McPherson. A model for volume lighting and modeling. *IEEE Trans. Visualization and Computer Graphics*, 9(2):150–162, April 2003.

[16] J. Krueger and R. Westermann. Acceleration techniques for gpu-based volume rendering. In *Proc. IEEE Visualization*, pages 287–292, 2003.

[17] M. Magnor, G. Kindlmann, C. Hansen, and N. Duric. Constrained inverse volume rendering for planetary nebulae. In *Proc. IEEE Visualization*, pages 83–90, October 2004.

[18] N. Max. Optical models for direct volume rendering. *IEEE Trans. Visualization and Computer Graphics*, 1(2):99–108, 1995.

[19] D. Nadeau and E. Engquist. Volume visualization of the evolution of an emission nebula. <http://vis.sdsc.edu/research/hayden2.html>, 2002.

[20] D. Nadeau, J. Genetti, S. Napear, B. Pailthorpe, C. Emmart, E. Wesselak, and D. Davidson. Visualizing stars and emission nebulae. *Computer Graphics Forum*, 20(1):27–33, March 2001.

[21] K. Perlin. An image synthesizer. *Proc. ACM Conference on Computer Graphics (SIGGRAPH'85)*, pages 287–296, 1985.

[22] S. Premoze, M. Ashikhmin, and P. Shirley. Path integration for light transport in volumes. In *Proc. Eurographics Symposium on Rendering (EGSR'03)*, pages 52–63, 2003.

[23] K. Riley, D. Ebert, M. Kraus, J. Tessendorf, and C. Hansen. Efficient rendering of atmospheric phenomena. In *Proc. Eurographics Symposium on Rendering (EGSR'04)*, pages 375–386, 2004.

[24] H. Rushmeier and K. Torrance. The zonal method for calculating light intensities in the presence of a participating medium. *ACM Trans. on Computer Graphics*, 21:293–302, July 1987.

[25] H. Scharsach. Advanced GPU raycasting. In *Central European Seminar on Computer Graphics (CESG'05)*, 2005. <http://www.cg.tuwien.ac.at/studentwork/CESCG/proceedings.html>.

[26] K. Sellgren, M. Werner, and H. Dinerstein. Scattering of infrared radiation by dust in NGC 7023 and NGC 2023. *Astrophysical Journal*, 400:238–247, November 1992.

[27] J. Stam. Multiple scattering as a diffusion process. *Proc. Eurographics Rendering Workshop (EGRW'95)*, pages 51–58, June 1995.

[28] T. and D. Hallas. Gallery of astrophotography – nebulae. <http://www.astrophoto.com/GalleryNebulae.htm>, 2005.

[29] H. van de Hulst. *Light Scattering by Small Particles*. Dover Publications, Inc., New York, 1982.

[30] A. Witt and R. Schild. CCD surface photometry of bright reflection nebulae. *Astrophysical Journal Supplement Series*, 62:839–852, December 1986.

[31] A. Witt, G. Walker, R. Bohlin, and T. Stecher. The scattering phase function of interstellar grains: The case of the reflection nebula NGC 7023. *Astrophysical Journal*, 261:492–509, October 1982.

[32] W. Zheng and C. O'Dell. A three-dimensional model of the Orion nebula. *Astrophysical Journal*, 438(2):784–793, January 1995.

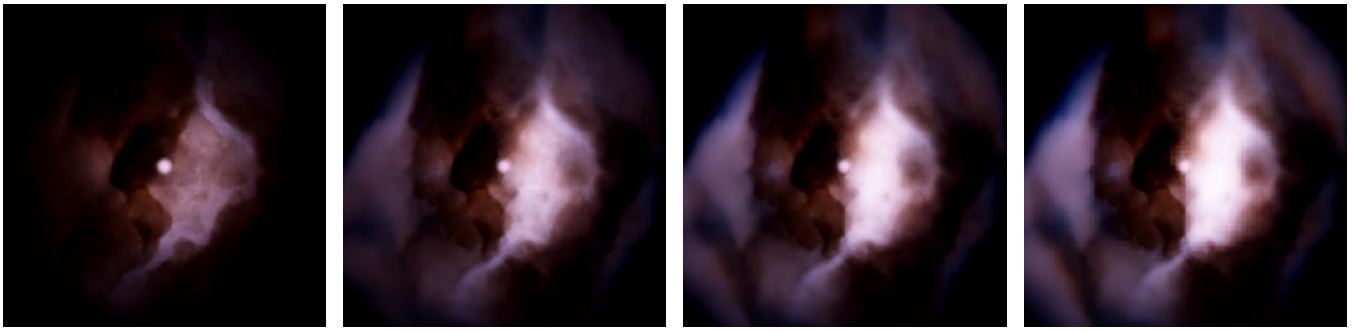


Figure 9: Wide-range multiple scattering: To include global multiple scattering effects, a multi-resolution rendering approach is pursued. From left to right, the images show the effect when taking $n = 0, 1, 2$ and 3 resolution levels into account (all images linear gamma, identical range).

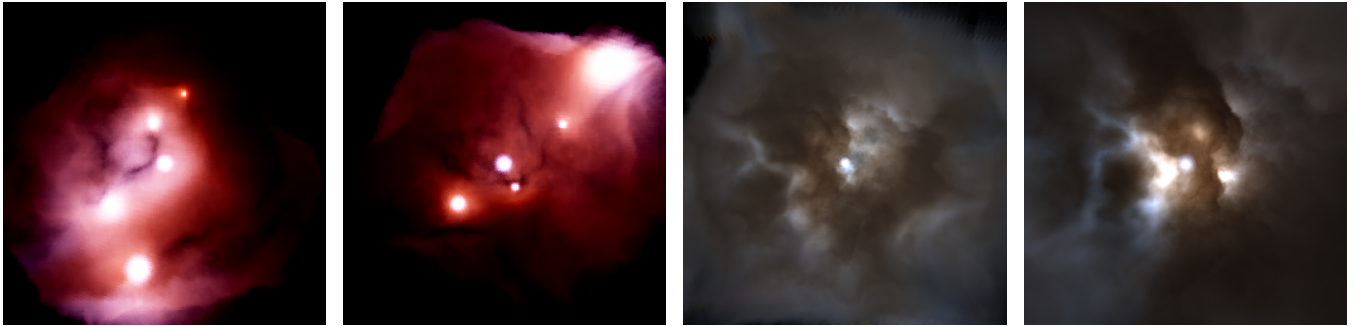


Figure 10: Screenshots from a fly-around sequence of a nebula illuminated by five stars (left), and images of a fly-through sequence with a single central star (right). Left: From the outside, nebulae appear reddish due to wavelength-dependent extinction. Right: Once inside the nebula, thin dust backscatters predominantly blue light, while light backscattered from dense dust assumes the color of the illuminating star.

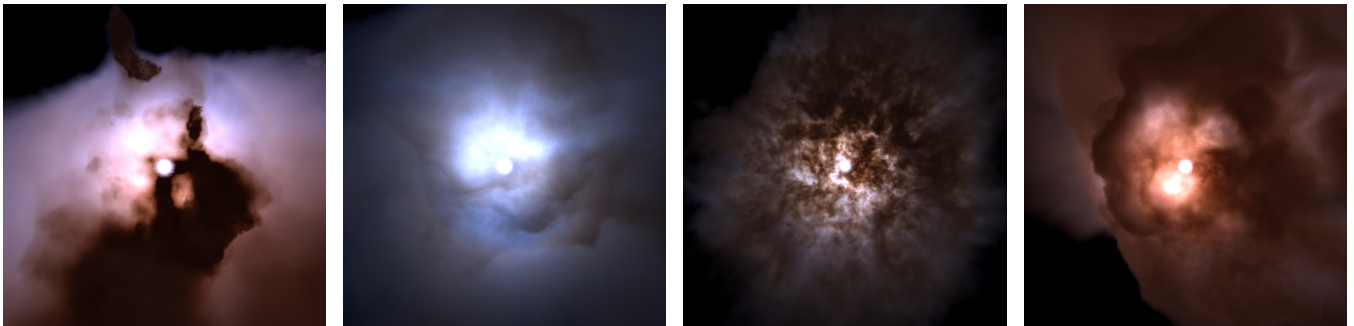


Figure 11: Renditions of different 3D dust distributions.

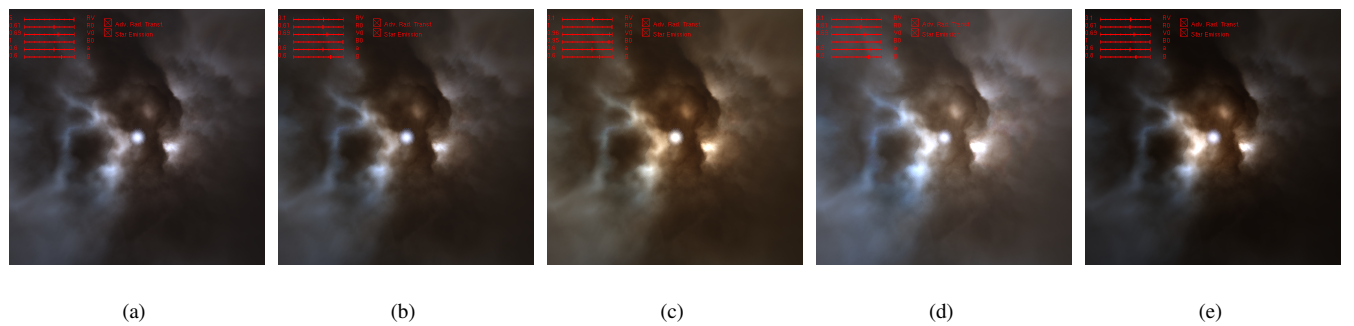


Figure 12: Varying physical parameters: (a) visualization for the standard values $a = 0.6$, $g = 0.6$, $R_V = 5$, and an illuminating O-class star; (b) same as (a), but $R_V = 3.1$; (c) same as (a), but for an illuminating star similar to our Sun (G2V-class); (d) same as (a), but $a = 0.8$; (e) same as (a), but $g = 0.8$.